
Proceedings Paper:
Nejad, S., Gladwin, D.T. orcid.org/0000-0001-7195-5435 and Stone, D.A. orcid.org/0000-0002-5770-3917 (2016) On-chip implementation of Extended Kalman Filter for adaptive battery states monitoring. In: IECON 2016 - 42nd Annual Conference of the IEEE Industrial Electronics Society. IIECON 2016 - 42nd Annual Conference of the IEEE Industrial Electronics Society , 24/07/2016 - 27/ 07/2016, Florence, Italy. Institute of Electrical and Electronics Engineers , pp. 5513-5518. ISBN 9781509034741

https://doi.org/10.1109/IECON.2016.7793527

On-Chip Implementation of Extended Kalman Filter For Adaptive Battery States Monitoring

S.Nejad, D. T. Gladwin and D. A. Stone
Department of Electronic and Electrical Engineering
University of Sheffield
Sheffield, United Kingdom
S.Nejad@Sheffield.ac.uk

***Abstract*—This paper reports the development and implementation of an adaptive lithium-ion battery monitoring system. The monitoring algorithm is based on the nonlinear Dual Extended Kalman Filter (DEKF), which allows for simultaneous states and parameters estimation. The hardware platform consists of an ARM cortex-M0 processor with six embedded analogue-to-digital converters (ADCs) for data acquisition. Two definitions for online state-of-health (SOH) characterisation are presented; one energy-based and one power-based. Moreover, a method for online estimation of battery's capacity, which is used in SOH characterisation is proposed. Two definitions for state-of-power (SOP) are adopted. Despite the presence of large sensor noise and incorrect filter initialisation, the DEKF algorithm poses excellent SOC and SOP tracking capabilities during a dynamic discharge test. The SOH prediction results are also in good agreement with actual measurements.**

Keywords—Lithium-ion; Adaptive; Battery Monitoring System; State-of-Charge; State-of-Health; State-of-Power; Estimation

I. INTRODUCTION

Lithium-ion batteries power a wide range of applications such as in electric vehicles (EVs), unmanned aerial vehicles (UAVs) and grid-tie energy storage. To enhance the safety performance and to prolong the battery's service life, battery management systems (BMSs) are developed and utilised as an integral solution. A typical BMS comprises of two operational facets; monitoring the battery's operating conditions and controlling the drive circuit accordingly [1]. The purpose of the monitoring system is to ensure that the battery does not incur any permanent damage due to over-rated currents and voltages, or undesirable levels of charge. To this end, various battery states including state-of-charge (SOC), state-of-health (SOH) and state-of-power (SOP) must be accurately predicted online.

The simplest approach to estimate SOC is by integrating the terminal current with respect to charge/discharge period. This is called the "coulomb-counting" method. Similarly, SOH and SOP can be jointly predicted using a technique so-called electrochemical impedance spectroscopy (EIS) [2]. Although, great accuracies are achievable with EIS, it is a laborious and costly technique that can only be executed offline. Moreover, the coulomb-counting method for SOC estimation suffers largely from accumulative sensor noise and initialisation-induced errors. As a result, researchers have developed various model-based techniques that can be used to accurately predict and monitor the aforementioned battery states online.

Table I provides a list of the most reported online estimators in literature for BMS applications. These estimators are often combined with a suitable model representation of the battery system in order to adapt to the nonlinearities inherent to the battery dynamics. Whereas Fuzzy Logic [3] and Artificial Neural Network [4] estimators require large model-training datasets, those observer-based estimators, such as sliding-mode observer [5], may suffer from lack of persistence of excitation of battery input/output signals [6].

Alternatively, the Extended Kalman Filter (EKF) [7] – a recursive algorithm used for online identification of nonlinear systems – can be employed to estimate SOC, SOH and SOP in real time. To compensate for the time-variability of battery parameters due to SOC modification and SOH degradation, a second EKF is usually designed to simultaneously identify the underlying nonlinear parameters. This forms the basis of the robust dual-EKF (DEKF) estimator that is applied in solving many BMS problems (e.g. [8]–[10]).

TABLE I
COMPARISON OF ONLINE ESTIMATORS FOR BMS USE

Technique	SOC	SOH	SOP
Fuzzy Logic	✓	✓	
Sliding-Mode Observer	✓	✓	
Artificial Neural Network	✓	✓	✓
Dual Extended Kalman Filter	✓	✓	✓

Most BMS algorithms reported in literature are developed and verified with laboratory-based experiments. This is achieved by measuring the battery voltage and current using highly accurate lab equipment. The acquired data is then processed either online or offline, using PC-based software packages such as MATLAB and LabVIEW as an implementation platform. Therefore, in this work, the development of a low-cost battery monitoring system that is suitable for online BMS verification purposes, is reported. The proposed system features a microprocessor unit (MCU), which is utilised as a standalone platform for the DEKF algorithm to perform SOC, SOP, and SOH estimation in real time.

II. Battery Modelling and State Estimation

A. Equivalent Electrical-Circuit Model

A second-order RC network model [11] is adopted herein to describe the dynamics of the battery/cell under operation. The model structure, as depicted in Fig. 1, is comprised of an ideal voltage source that represents the battery/cell's open-circuit voltage (OCV) as a function of SOC, an uncompensated series-resistor element R_s and two RC branches that capture the short time-constant voltage drops associated with the charge-transfer resistance and double-layer capacitance at the electrodes (V_{stc}) and the long time-constant diffusional processes (V_{ltc}) respectively.

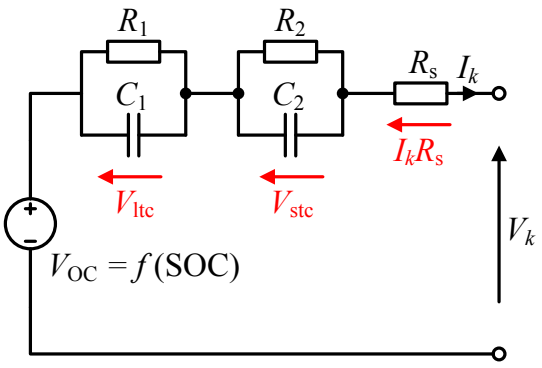

Fig. 1. Second-order RC battery model structure

B. State-of-Charge Estimation

Here, SOC is defined as the ratio of available ampere-hour charge measured using the coulomb-counting method, with respect to the maximum available battery capacity C_{max}.

$$\mathrm{SOC}_{k+1} = \mathrm{SOC}_k - \frac{\eta I_k \Delta t}{Q_{\max}} \tag{1}$$

where $Q_{\max} = 3600 \times C_{\max}$; Δt is the sampling period; η is the battery's coulombic efficiency; and I_k is input current.

C. Open-Circuit Voltage Estimation

The OCV is defined as the battery's terminal voltage that is measured after a very long period of zero-current relaxation. In practice, the OCV at a particular SOC is generally measured based on the first few hours of load disconnection. A pulsed-current test, similar to that reported in [8], is conducted at 25 °C to extract the charge and discharge OCV curves as a function of SOC. A current level of 0.5 C is used to charge/discharge the battery under test in steps of ΔSOC = 10%. The current pulses are separated by one-hour relaxation intervals, which is long enough for most lithium-ion battery chemistries to reach an equilibrium state.

The OCV results obtained for a 3.6 Ah cylindrical lithium-ion nickel manganese cobalt oxide (LiNMC) test cell are presented in Fig. 2. For most energy storage applications with regenerative currents, the battery's SOC is usually confined to a useable operating range of ~20 to 80%. Over this range, a third-order polynomial (as fitted in Fig. 2) can sufficiently describe the average OCV-SOC relationship for a typical 3.6 Ah LiNMC test cell. This is expressed as,

$$V_{\mathrm{OC}} = p_3 \times \mathrm{SOC}^3 + p_2 \times \mathrm{SOC}^2 + p_1 \times \mathrm{SOC} + p_0 \tag{2}$$

where coefficients p_0, p_1, p_2 and p_3 are experimentally determined. In this work, the OCV-SOC relationship is established at an ambient temperature of 25 °C.

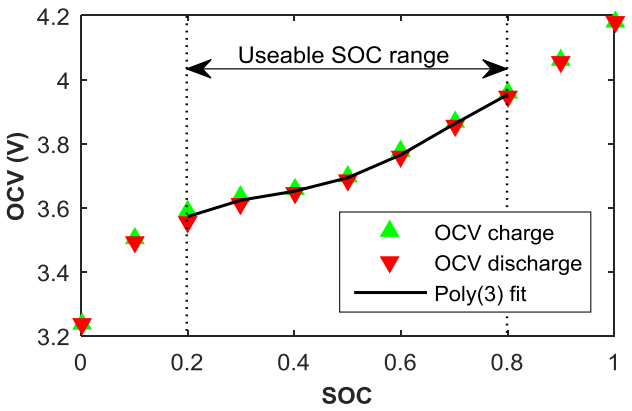

Fig. 2. OCV-SOC relationship for a lithium-ion NMC cell, showing third-order polynomial curve-fit over the useable SOC range

D. State-of-Power Estimation

The SOP definition used here is similar to that reported in [11], which is related to the available sink/source power over a short period of Δt seconds. Subsequently, the discharge P_k^{dis} and charge P_k^{ch} powers at time-step k can be defined as,

$$P_k^{\mathrm{dis}} = \frac{V_{\min}\left(\hat{V}_{\mathrm{OC},k} - V_{\min}\right)}{\hat{R}_s + \hat{R}_1 + \hat{R}_2} \tag{3}$$

$$P_k^{\mathrm{ch}} = \frac{V_{\max}\left(V_{\max} - \hat{V}_{\mathrm{OC},k}\right)}{\hat{R}_s + \hat{R}_1 + \hat{R}_2}. \tag{4}$$

In (3) and (4), $V_{\min}$ and $V_{\max}$ are the minimum and maximum battery threshold voltages specified for a safe operation. $\hat{R}_s$, $\hat{R}_1$ and $\hat{R}_2$ are predictions for the resistive elements in Fig. 1 and $\hat{V}_{\mathrm{OC}}$ is an estimate for the battery's OCV at time-step k. Consequently, using (3) and (4), a power-based definition for the battery's functionality or state-of-function (SOF) is developed.

$$\mathrm{SOF} = \begin{cases} 1, & \text{for } P_k^{\mathrm{ch}} \geq P_{\mathrm{req}}^{\mathrm{ch}} \text{ and } P_k^{\mathrm{dis}} \geq P_{\mathrm{req}}^{\mathrm{dis}} \\ 0, & \text{for } P_k^{\mathrm{ch}} < P_{\mathrm{req}}^{\mathrm{ch}} \text{ and } P_k^{\mathrm{dis}} < P_{\mathrm{req}}^{\mathrm{dis}} \end{cases} \tag{5}$$

where $P_{\mathrm{req}}^{\mathrm{ch}} = I_{\mathrm{req}}^{\mathrm{ch}} \times V_{\max}$ and $P_{\mathrm{req}}^{\mathrm{dis}} = I_{\mathrm{req}}^{\mathrm{dis}} \times V_{\min}$ are respectively the quantities of required charge or discharge power in order to fulfil a particular task. In order to verify the charge and discharge SOP definitions given in this paper, a hybrid pulse power characterisation (HPPC) test [12] is performed on the LiNMC test cell at 25 °C.

E. State-of-Health Estimation

There are two distinct definitions for SOH in literature relating it to either a power or energy fade. The source/sink power capability of a battery largely depends on its internal resistance. As the resistance grows with ageing, the battery's instantaneous available power fades away. Moreover, as the battery ages, it loses some of its ampere-hour capacity, leading to an energy fade.

Thus, to establish a comprehensive battery state monitoring system, in this paper, both definitions of SOH as given by (6) and (7) are considered.

$$\mathrm{SOH}_{\mathrm{pwr}} = 1 - \left(\frac{R^{\mathrm{s}}_{\mathrm{now}} - R^{\mathrm{s}}_{0}}{R^{\mathrm{s}}_{0}}\right) \times 100\% \tag{6}$$

$$\mathrm{SOH}_{\mathrm{enr}} = \frac{C^{\mathrm{Ah}}_{\mathrm{now}}}{C^{\mathrm{Ah}}_{0}} \times 100\% \tag{7}$$

where $\mathrm{SOH}_{\mathrm{pwr}}$ is a power-based definition, relating the battery's current series resistance $R^{\mathrm{s}}_{\mathrm{now}}$ to that of a reference value R^{s}_{0}; $\mathrm{SOH}_{\mathrm{enr}}$ is an energy-based definition, which is the ratio of the battery's current capacity $C^{\mathrm{Ah}}_{\mathrm{now}}$ in ampere-hour to that of a reference value C^{Ah}_{0}. The reference quantities R^{s}_{0} and C^{Ah}_{0} can either be determined experimentally at the beginning of the battery's life (i.e. $j = 0$) at 25 °C, or they can be exported from the manufacture's datasheet.

In order to predict C^{Ah}_{j} without performing a full charge/discharge cycle, a new method is proposed. During a charge/discharge cycle, the quantity of coulombic charge in the battery is modified according to (8).

$$Q_{\mathrm{mod}} = Q_{\alpha} - Q_{\beta} = Q_{\alpha} - \sum_{k=\alpha}^{\beta} I_k \cdot \Delta t \tag{8}$$

where Q_{α} is the initial charge at discrete time-step $k = \alpha$ and Q_{β} is the final charge value at $k = \beta$. For short-time intervals of charge/discharge cycles (i.e. seconds to minutes), Q_{β} can be calculated using the integral of the current-sensor measurements. The short time reduces any sensor-induced errors during current integration. The SOC is also modified as,

$$\mathrm{SOC}_{\mathrm{mod}} = \mathrm{SOC}_{\alpha} - \mathrm{SOC}_{\beta}. \tag{9}$$

Now, considering the definition of SOC given in (1), and assuming an accurate estimate for $\mathrm{SOC}_{\mathrm{mod}}$ is available during the charge modification Q_{mod}, the battery's ampere-hour capacity in real time can be predicted by,

$$\hat{C}_{\mathrm{Ah}} = \frac{Q_{\mathrm{mod}}}{3600 \times \mathrm{SOC}_{\mathrm{mod}}}. \tag{10}$$

III. Dual Extended Kalman Filter Algorithm

A. Battery State-Space Equations

By using standard techniques, the state-space equations for the battery model depicted in Fig. 1 are derived.

$$\begin{aligned}
\boldsymbol{f}(\cdot) &= \begin{bmatrix} x_1 \\ x_2 \\ x_3 \end{bmatrix} = \begin{bmatrix} \mathrm{SOC}_{k+1} \\ V_{\mathrm{ltc}_{k+1}} \\ V_{\mathrm{stc}_{k+1}} \end{bmatrix} \\
&= \begin{bmatrix} 1 & 0 & 0 \\ 0 & e^{\frac{-\Delta t}{\tau_1}} & 0 \\ 0 & 0 & e^{\frac{-\Delta t}{\tau_2}} \end{bmatrix} \begin{bmatrix} \mathrm{SOC}_{k} \\ V_{\mathrm{ltc}_{k}} \\ V_{\mathrm{stc}_{k}} \end{bmatrix} \\
&+ \begin{bmatrix} -\dfrac{\eta \Delta t}{Q_{\mathrm{max}}} & 0 & 0 \\ 0 & R_1\left(1 - e^{\frac{-\Delta t}{\tau_{\mathrm{ltc}}}}\right) & 0 \\ 0 & 0 & R_2\left(1 - e^{\frac{-\Delta t}{\tau_{\mathrm{stc}}}}\right) \end{bmatrix} I_k \\
\boldsymbol{\theta}_k &= [R_{\mathrm{s}}, R_1, \tau_{\mathrm{ltc}}, R_2, \tau_{\mathrm{stc}}]^{\mathrm{T}} \\
\boldsymbol{h}(\cdot) &= V_k = V_{\mathrm{OC}}(\mathrm{SOC}_k) - V_{\mathrm{ltc}_k} - V_{\mathrm{stc}_k} - I_k R_{\mathrm{s}}
\end{aligned} \tag{11}$$

where $\boldsymbol{f}(\cdot)$ and $\boldsymbol{h}(\cdot)$ are the nonlinear state transition and observation models respectively and $\tau_{\mathrm{ltc}} = R_1 C_1$ and $\tau_{\mathrm{stc}} = R_2 C_2$ are the transient time-constants.

Now, assuming the state filter gain $\mathbf{L}^{\mathrm{x}}_k$ is weakly related to $\boldsymbol{\theta}_k$, the Jacobian matrices required for the recursive DEKF algorithm presented in Table II can be computed as,

$$\mathbf{F}_{k-1} = \left.\frac{\partial \boldsymbol{f}(\cdot)}{\partial \mathbf{x}_k}\right|_{\mathbf{x}_k = \hat{\mathbf{x}}^{+}_{k-1}} = \begin{bmatrix} 1 & 0 & 0 \\ 0 & e^{\frac{-\Delta t}{\tau_1}} & 0 \\ 0 & 0 & e^{\frac{-\Delta t}{\tau_2}} \end{bmatrix} \tag{12}$$

$$\mathbf{H}^{\mathrm{x}}_k = \left.\frac{\partial \boldsymbol{h}(\cdot)}{\partial \mathbf{x}_k}\right|_{\mathbf{x}_k = \hat{\mathbf{x}}^{-}_k} = [\partial V_{\mathrm{OC}}/\partial \mathrm{SOC}_k \quad -1 \quad -1] \tag{13}$$

$$\left.\begin{aligned}
\mathbf{H}^{\theta}_k &= \left.\frac{\mathrm{d}h(\cdot)}{\mathrm{d}\boldsymbol{\theta}_k}\right|_{\boldsymbol{\theta}_k = \hat{\boldsymbol{\theta}}^{-}_k} = \frac{\partial \boldsymbol{h}(\cdot)}{\partial \hat{\boldsymbol{\theta}}^{-}_k} + \frac{\partial \boldsymbol{h}(\cdot)}{\partial \hat{\mathbf{x}}^{-}_k} \cdot \frac{\mathrm{d}\hat{\mathbf{x}}^{-}_k}{\mathrm{d}\hat{\boldsymbol{\theta}}^{-}_k} \\
\frac{\mathrm{d}\hat{\mathbf{x}}^{-}_k}{\mathrm{d}\hat{\boldsymbol{\theta}}^{-}_k} &= \frac{\partial \boldsymbol{f}(\cdot)}{\partial \hat{\boldsymbol{\theta}}^{-}_k} + \frac{\partial \boldsymbol{f}(\cdot)}{\partial \hat{\mathbf{x}}^{+}_{k-1}} \cdot \frac{\mathrm{d}\hat{\mathbf{x}}^{+}_{k-1}}{\mathrm{d}\hat{\boldsymbol{\theta}}^{-}_k} \\
\frac{\partial \boldsymbol{h}(\cdot)}{\partial \hat{\boldsymbol{\theta}}^{-}_k} &= [-I_{k-1} \quad 0 \quad 0 \quad 0 \quad 0] \\
\frac{\mathrm{d}\hat{\mathbf{x}}^{-}_k}{\mathrm{d}\hat{\boldsymbol{\theta}}^{-}_k} &= \begin{bmatrix} 0 & 0 & 0 & 0 & 0 \\ 0 & a_{2,2} & a_{2,3} & 0 & 0 \\ 0 & 0 & 0 & a_{3,4} & a_{3,5} \end{bmatrix}
\end{aligned}\right\} \tag{14}$$

where,

$a_{2,2} = -I_{k-1} \cdot (\exp(\Delta t/\tau^2_{\mathrm{ltc}}) - 1)$;
$a_{2,3} = (\Delta t/\tau^2_{\mathrm{ltc}}) \cdot \left(\hat{x}^{-}_{2,k} - R_1 I_{k-1}\right) \exp(-\Delta t/\tau_{\mathrm{ltc}})$;
$a_{3,4} = -I_{k-1} \cdot (\exp(\Delta t/\tau^2_{\mathrm{stc}}) - 1)$; and
$a_{3,5} = (\Delta t/\tau^2_{\mathrm{stc}}) \cdot \left(\hat{x}^{-}_{3,k} - R_2 I_{k-1}\right) \exp(-\Delta t/\tau_{\mathrm{stc}})$.

B. Underlying Theory

The state-space equations for the states filter are given as,

$$\begin{aligned} \mathbf{x}_{k+1} &= f(\mathbf{x}_k, \mathbf{u}_k, \boldsymbol{\theta}_k) + \mathbf{w}_k \\ \mathbf{y}_k &= h(\mathbf{x}_k, \mathbf{u}_k, \boldsymbol{\theta}_k) + \mathbf{v}_k \\ \mathbf{w}_k &\sim N(0, \mathbf{Q}_k^{\mathrm{x}}) \\ \mathbf{v}_k &\sim N(0, \mathbf{R}_k^{\mathrm{x}}) \end{aligned} \tag{15}$$

where $\mathbf{x}_k \in \mathbb{R}^n$ is a the states vector, $\boldsymbol{\theta}_k \in \mathbb{R}^q$ is the time-varying parameters vector; $\mathbf{w}_k \in \mathbb{R}^n$ and $\mathbf{v}_k \in \mathbb{R}^m$ are the zero-mean process and measurement noises of covariance $\mathbf{Q}_k^{\mathrm{x}}$ and $\mathbf{R}_k^{\mathrm{x}}$ respectively; $f(\cdot,\cdot,\cdot)$ is a nonlinear function that evolves the state estimates from $\mathbf{x}_k$ to $\mathbf{x}_{k+1}$ in discrete time-steps; and $h(\cdot,\cdot,\cdot)$ is a nonlinear function that maps the state estimates into the observed space.

Similarly, for the EKF parameters, the state-space equations are defined as,

$$\begin{aligned} \boldsymbol{\theta}_{k+1} &= \boldsymbol{\theta}_k + \mathbf{r}_k \\ \mathbf{d}_k &= h(\mathbf{x}_k, \mathbf{u}_k, \boldsymbol{\theta}_k) + \mathbf{e}_k \\ \mathbf{r}_k &\sim N(0, \mathbf{Q}_k^{\theta}) \\ \mathbf{e}_k &\sim N(0, \mathbf{R}_k^{\theta}) \end{aligned} \tag{16}$$

$\mathbf{r}_k \in \mathbb{R}^p$ is a small white noise of covariance $\mathbf{Q}_k^{\theta}$ that evolves the parameters over time; the output equation $\mathbf{d}_k \in \mathbb{R}^m$ is given as a measurable function of $\boldsymbol{\theta}_k$ and a white noise $\mathbf{e}_k \in \mathbb{R}^m$ of covariance $\mathbf{R}_k^{\theta}$ to account for the sensor noise and modelling uncertainties. The equations for the recursive identification of $\mathbf{x}_k$ and $\boldsymbol{\theta}_k$ are summarised in Table II.

TABLE II
DUAL-EKF ALGORITHM FOR ONLINE BATTERY STATE AND PARAMETER IDETIFICATION

Initialisation:

$\hat{\mathbf{x}}_0^+ = [0.2, 0, 0]^{\mathrm{T}}$, $\quad \hat{\boldsymbol{\theta}}_0^+ = [0.02, 0.01, 100, 0.01, 10]^{\mathrm{T}}$

$\mathbf{Q}_0^{\mathrm{x}} = \mathrm{diag}_n\{1 \times 10^{-8}\}$, $\quad \mathbf{P}_{\hat{\mathrm{x}},0}^+ = \mathrm{diag}_n\{10\}$, $\quad \mathbf{R}_0^{\mathrm{x}} = \mathrm{diag}_m\{10\}$

$\mathbf{Q}_0^{\theta} = \mathrm{diag}_q\{1 \times 10^{-8}\}$, $\quad \mathbf{P}_{\hat{\theta},0}^+ = \mathrm{diag}_q\{10\}$, $\quad \mathbf{R}_0^{\theta} = \mathrm{diag}_m\{10\}$

Time-update equations:

$\hat{\mathbf{x}}_k^- = f(\hat{\mathbf{x}}_{k-1}^+, \mathbf{u}_{k-1}, \hat{\boldsymbol{\theta}}_k^-)$, $\quad \hat{\boldsymbol{\theta}}_k^- = \hat{\boldsymbol{\theta}}_{k-1}^+$

$\mathbf{P}_{\hat{\mathrm{x}},k}^- = \mathbf{F}_{k-1}\mathbf{P}_{\hat{\mathrm{x}},k-1}^+\mathbf{F}_{k-1}^T + \mathbf{Q}_k^{\mathrm{x}}$, $\quad \mathbf{P}_{\hat{\theta},k}^- = \mathbf{P}_{\hat{\theta},k-1}^+ + \mathbf{Q}_k^{\theta}$

Measurement-update equations:

$\mathbf{L}_k^{\mathrm{x}} = \mathbf{P}_{\hat{\mathrm{x}},k}^-(\mathbf{H}_k^{\mathrm{x}})^T\left[\mathbf{H}_k^{\mathrm{x}}\mathbf{P}_{\hat{\mathrm{x}},k}^-(\mathbf{H}_k^{\mathrm{x}})^T + \mathbf{R}_k^{\mathrm{x}}\right]^{-1}$

$\hat{\mathbf{x}}_k^+ = \hat{\mathbf{x}}_k^- + \mathbf{L}_k^{\mathrm{x}}\left[\mathbf{y}_k - h(\hat{\mathbf{x}}_k^-, \mathbf{u}_k, \hat{\boldsymbol{\theta}}_k^-)\right]$

$\mathbf{P}_{\hat{\mathrm{x}},k}^+ = (\boldsymbol{I} - \mathbf{L}_k^{\mathrm{x}}\mathbf{H}_k^{\mathrm{x}})\mathbf{P}_{\hat{\mathrm{x}},k}^-(\boldsymbol{I} - \mathbf{L}_k^{\mathrm{x}}\mathbf{H}_k^{\mathrm{x}})^T + \mathbf{L}_k^{\mathrm{x}}\mathbf{R}_k^{\mathrm{x}}(\mathbf{L}_k^{\mathrm{x}})^T$

$\mathbf{L}_k^{\theta} = \mathbf{P}_{\hat{\theta},k}^-(\mathbf{H}_k^{\theta})^T\left[\mathbf{H}_k^{\theta}\mathbf{P}_{\hat{\theta},k}^-(\mathbf{H}_k^{\theta})^T + \mathbf{R}_k^{\theta}\right]^{-1}$

$\hat{\boldsymbol{\theta}}_k^+ = \hat{\boldsymbol{\theta}}_k^- + \mathbf{L}_k^{\theta}\left[\mathbf{d}_k - h(\hat{\mathbf{x}}_k^-, \mathbf{u}_k, \hat{\boldsymbol{\theta}}_k^-)\right]$

$\mathbf{P}_{\hat{\theta},k}^+ = \left(\boldsymbol{I} - \mathbf{L}_k^{\theta}\mathbf{H}_k^{\theta}\right)\mathbf{P}_{\hat{\theta},k}^-\left(\boldsymbol{I} - \mathbf{L}_k^{\theta}\mathbf{H}_k^{\theta}\right)^T + \mathbf{L}_k^{\theta}\mathbf{R}_k^{\theta}\left(\mathbf{L}_k^{\theta}\right)^T$

IV. BATTERY MONITORING SYSTEM DEVELOPMENT

A. Software Configuration

The process flow-chart for the developed battery monitoring system is illustrated in Fig. 3. It starts by initialising the DEKF algorithm with the parameters given in Table II. The value of Q_{max} in (11) is initially set to the battery's nominal capacity. Thereafter, battery data (i.e. voltage, current and temperature) are acquired and fed into the DEKF algorithm every Δt seconds. Upon the completion of DEKF measurement-update at time-step k, SOC, OCV and RC model parameters are estimated. Then, the updated estimates are used in Equations (2)–(6) to calculate SOP, SOF and $\mathrm{SOH_{pwr}}$. Since the capacity C_{max} is a very slow time-varying parameter, it is predicted every 10 minutes, which is employed to update Q_{max} in (11) and predict $\mathrm{SOH_{enr}}$. Finally, the estimated states and parameters are sent to a PC over serial communication for storage and *in situ* user interface.

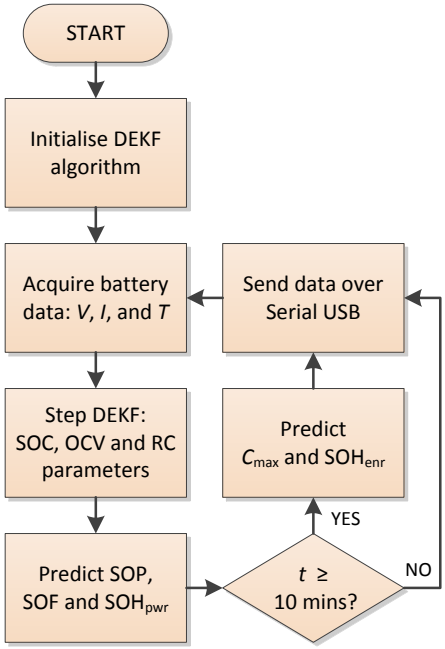

Fig. 3. Flow chart showing software structure for battery states estimation

B. Hardware Configuration

As depicted in Fig. 4, the developed system consists of an ARM Cortex-M0 processor (NXP KL25z128) with six embedded 16-bit analogue-to-digital-converters (ADCs). Battery current is measured using a bidirectional Hall-effect sensor (Allegro ACS712-20A), which outputs a proportional positive/negative analogue voltage for discharge/charge currents respectively. The battery surface temperature is measured using a 10 kΩ thermistor, which is calibrated using the Steinhart-Hart equation. The data acquisition is performed at 10 Hz. Prior to digital conversion of the analogue signals, they are conditioned accordingly; this involves an intermediate amplification stage that ensures the input signals are within the MCU's operating voltage range of 0–3.3 V; and a low-pass filter stage (corner frequency = 1 kHz) is added to remove any high-frequency noise contents.

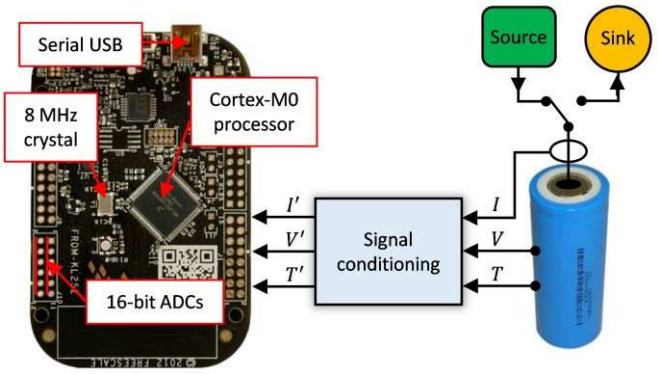

Fig. 4. Hardware configuration for embedded battery monitoring system

V. Experimental Verification

In order to verify the developed battery monitoring system, a dynamic test based on the Artemis [13] EV dive cycle is devised and implemented on a multi-channel Maccor battery tester. The test profile is comprised of a full charge/discharge cycle to measure the cell's actual capacity. Then, using a 0.5 C discharge current, SOC is moved from 100% to an initial level of 80% (typical in EV applications), followed by a 30 minute rest period. Thereafter, the cell is applied with approximately 28 repetitions of the Artemis-based current profile (as shown in Fig. 5.) to dynamically move SOC from 80% to 20%. All the tests are performed at a controlled temperature of 25 °C.

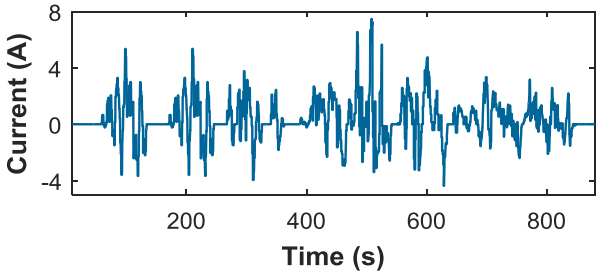

Fig. 5. Single repetition of Artemis-based dynamic current profile

Fig. 6 presents the measured terminal voltage and the predicted OCV for the 3.6 Ah LiNMC test cell, during the dynamic stress testing. Fig. 7 displays the DEKF identified model parameters R_s, R_1 and R_2 and their variations with SOC. Generally, as SOC decreases, the over-potential gradient between the positive and negative electrodes grows. This explains the increasing trend of R_s as observed in Fig. 7. During the first 30 minutes, whilst the battery is in open-circuit mode, the parameter EKF produces unrealistic negative estimates. This is due to the lack of persistence of excitation of the input signals. However, as soon as the load is engaged, the algorithm starts to converge towards the 'true' estimates.

Subsequently, the predicted OCV and predicted parameters $\hat{R}_s$, $\hat{R}_1$ and $\hat{R}_2$ are substituted into (3) and (4) at each time step to yield an instantaneous estimate for the available discharge and charge power respectively. The results are presented in Fig. 8. The available discharge power is calculated considering a minimum voltage threshold of 2.75 V, recommended by the cell manufacturer. Similarly, the amount of available charge power is obtained based on a maximum voltage limit of 4.2 V.

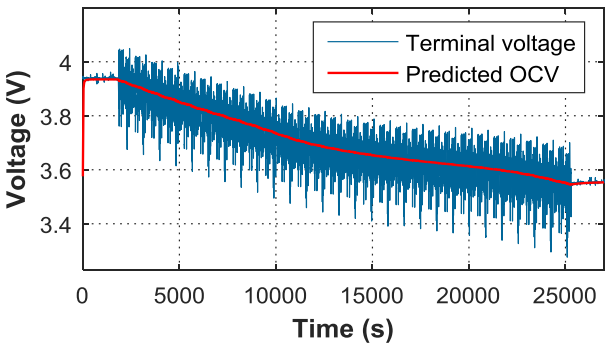

Fig. 6. Measured terminal voltage and predicted OCV

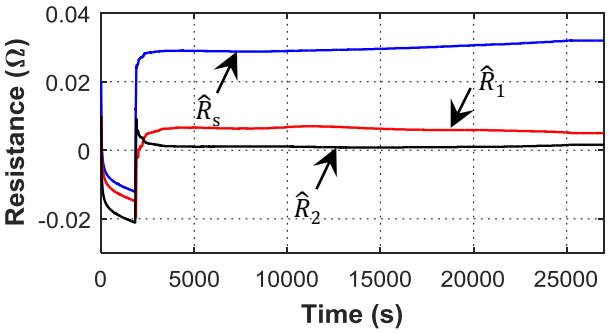

Fig. 7. DEKF identified model parameters R_s, R_1 and R_2

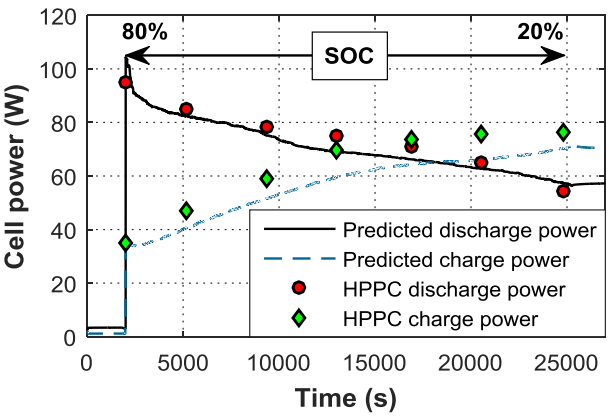

Fig. 8. Predicted instantaneous available discharge and charge power

Evidently, as SOC moves from 80% to 20%, the quantity of available discharge power drops, whilst the charge-accepting power of the cell increases. Over the active SOC range, it is determined that the LiNMC test cell can provide a minimum and maximum charge power of $P_{\min}^{\text{ch}} = 35$ W and $P_{\max}^{\text{ch}} = 70$ W, and a minimum and maximum discharge power of $P_{\min}^{\text{dis}} = 60$ W and $P_{\max}^{\text{dis}} = 90$ W respectively. These are in accordance with the HPPC results also presented in Fig. 8.

The cell's SOC is estimated by the EKF states filter and the results are presented in Fig. 9. To verify the convergence of the designed filter, the initial SOC is incorrectly set to 20%, whilst the true SOC = 79.57%. Without any prior knowledge of the cell's actual capacity, $Q_{\max}$ in (1) and (11) is set to a nominal

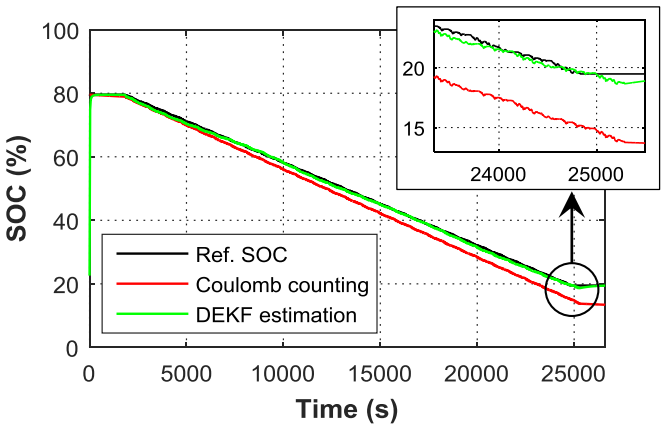

Fig. 9. Comparison of SOC estimated by DEKF and coulomb counting

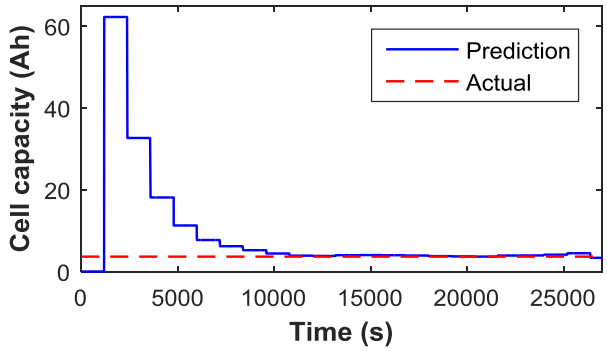

Fig. 10. Comparison of experimentally measured and predicted cell capacity

value of 3.6 Ah × 3600. Since the current sensor noise for the Maccor system is relatively small (±0.05% of full scale range), the integral of the cell current measured is used as a 'reference' for SOC comparison purposes.

As can be overserved in Fig. 9, the SOC calculated using the coulomb-counting method drifts away. This is due to the accumulation of sensor noise during the dynamic test period. As a result, the final SOC reported by the coulomb-counting method is measured at 14%, whilst the 'actual' SOC is 19.47%. On the other hand, despite the noisy measurements provided by the cheap current sensor and the incorrect initialisation, the DEKF algorithm achieves an excellent tracking of SOC.

In order to estimate the cell's current SOH level using the definitions given in (6) and (7), the initial capacity and resistance values are experimentally determined as $C_0^{\mathrm{Ah}} = 3.718\,\mathrm{Ah}$ and $R_0^{\mathrm{s}} = 0.028\,\Omega$. Using the accurately estimated SOC and the measured coulombic charge during a 10 minute window, cell capacity is predicted/updated. The arithmetic mode of the resulting capacity estimates is taken, yielding a value of $C_{now}^{\mathrm{Ah}} = 3.643\,\mathrm{Ah}$, whilst the actual capacity after a full charge/discharge cycle is determined to be 3.638 Ah. In addition, the cell's total resistance is identified by DEKF over the active SOC range as $R_{\mathrm{now}}^{\mathrm{s}} = 0.029\,\Omega$. Therefore, according to (6) and (7), the cell's SOH can be predicted and given as $\mathrm{SOH}_{\mathrm{enr}} = 97.85\%$ and $\mathrm{SOH}_{\mathrm{pwr}} = 96.43\%$, whilst actual $\mathrm{SOH} = 97.98\%$.

VI. Conclusions

In this paper, on-chip implementation of the recursive DEKF algorithm for adaptive lithium-ion battery monitoring has been reported. The developed system consisted of an ARM Cortex-M0 processor with embedded ADCs for data acquisition. The battery states of interest in this work included SOC, SOP and SOH. Subsequently, a method for online prediction of battery capacity for SOH characterisation has been proposed. Experimental data from a dynamic discharge test on a 3.6 Ah nominal capacity LiNMC cell was used for verification purposes. Despite the large current sensor drift and incorrect SOC initialisation, the DEKF algorithm posed excellent SOC and SOP tracking capabilities. These attributions are particularly important for those applications (e.g. in EVs and UAVs) requiring accurate SOC, SOP and SOH estimates for *in situ* implementation of various battery management strategies. Therefore, to prolong the battery/cell's lifetime, the proposed system can also be employed as a low-cost platform to perform the necessary control actions.

References

[1] H. Rahimi-Eichi, U. Ojha, F. Baronti, and M. Y. Chow, "BMS: An Overview of Its Application in the Smart Grid and Electric Vehicles," *IEEE Ind. Electron. Mag.*, vol. 7, no. 2, pp. 4–16, 2013.

[2] D. I. Stroe, M. Swierczynski, A. I. Stan, V. Knap, R. Teodorescu, and S. J. Andreasen, "Diagnosis of lithium-ion batteries state-of-health based on electrochemical impedance spectroscopy technique," in *Energy Conversion Congress and Exposition (ECCE), 2014 IEEE*, pp. 4576–4582, 2014.

[3] T. Ma, B. Serrano, and O. Mohammed, "Fuzzy logic based power and thermal management system design for multi-cell lithium-ion battery bank protection and operation," in *Power Systems Conference (PSC)*, pp. 1–5, 2014, *2014*.

[4] C. Fleischer, W. Waag, Z. Bai, and D. U. Sauer, "Self-learning state-of-available-power prediction for lithium-ion batteries in electrical vehicles," in *Vehicle Power and Propulsion Conference (VPPC), 2012 IEEE*, pp. 370–375, 2012.

[5] M. Gholizadeh and F. R. Salmasi, "Estimation of state of charge, unknown nonlinearities, and state of health of a lithium-ion battery based on a comprehensive unobservable model," *IEEE Trans. Ind. Electron.*, vol. 61, no. 3, pp. 1335–1344, 2014.

[6] V. V Chalam, *Adaptive Control Systems: Techniques and Applications*. New York: Marcel Dekker, Inc., 1987.

[7] R. G. Brown and P. Y. C. Hwang, *Introduction to Random Signals and Applied Kalman Filtering*, Third. New York, NY: John Wiley & Sons, Inc., 1997.

[8] S. Nejad, D. T. Gladwin, and D. A. Stone, "Enhanced state-of-charge estimation for lithium-ion iron phosphate cells with flat open-circuit voltage curves," in *Industrial Electronics Society, IECON 2015 - 41st Annual Conference of the IEEE*, pp. 3187–3192, 2015.

[9] F. Baronti, R. Roncella, R. Saletti, and W. Zamboni, "FPGA implementation of the mix algorithm for state-of-charge estimation of Lithium-ion batteries," in *Industrial Electronics Society, IECON 2014 - 40th Annual Conference of the IEEE*, pp. 5641–5646, 2014.

[10] R. R. Richardson and D. A. Howey, "Sensorless Battery Internal Temperature Estimation Using a Kalman Filter With Impedance Measurement," *IEEE Trans. Sustain. Energy*, vol. 6, no. 4, pp. 1190–1199, 2015.

[11] S. Nejad, D. T. Gladwin, and D. A. Stone, "A systematic review of lumped-parameter equivalent circuit models for real-time estimation of lithium-ion battery states," *J. Power Sources*, vol. 316, pp. 183–196, 2016.

[12] U.S. Department of Energy, "PNGV Battery Test Manual," 2001.

[13] T. Barlow, S. Latham, I. Mccrae, and P. Boulter, "A reference book of driving cycles for use in the measurement of road vehicle emissions," 2009.